Organic & Biomolecular Chemistry

Dynamic Article Links

Cite this: *Org. Biomol. Chem.*, 2012, **10**, 1014

www.rsc.org/obc

PAPER

The reaction mechanism of hydroxyethylphosphonate dioxygenase: a QM/MM study†

Likai Du, Jun Gao,* Yongjun Liu, Dongju Zhang and Chengbu Liu*

Received 21st July 2011, Accepted 26th October 2011
DOI: 10.1039/c1ob06221b

By employing *ab initio* quantum mechanical/molecular mechanical (QM/MM) and molecular dynamics (MD) simulations, we have provided further evidence against the previously proposed hydroperoxylation or hydroxylation mechanism of hydroxyethylphosphonate dioxygenase (HEPD). HEPD employs an interesting catalytic cycle based on concatenated bifurcations. The first bifurcation is based on the abstraction of hydrogen atoms from the substrate, which leads to a distal or proximal hydroperoxo species (Fe–OOH or Fe–(OH)O). The second and the third bifurcations refer to the carbon–carbon bond cleavage reaction. And this is achieved through a tridentate intermediate, or employing a proton-shuttle assisted mechanism, in which the residue Glu_{176} or the Fe^{IV}═O group serves as a general base. The reaction directions seem to be tunable and show significant environment dependence. This mechanism can provide a comprehensive interpretation for the seemingly contradicting experimental evidences and provide insight into the development of biochemistry and material sciences.

1. Introduction

Just like heme enzymes, dioxygen-activating mononuclear non-heme Fe^{II}-dependent enzymes catalyze a wide variety of reactions.[1–7] Since the development of sophisticated spectroscopic and computational approaches, significant advances have been made to probe and understand these non-heme enzymes.[3,8–15] A common structural motif of these non-heme enzymes is the 2-His-1-carboxylate facial triad binding the divalent iron, which is considered as a versatile platform for dioxygen activation.[1,6,14,16] In contrast to the porphyrin macrocycle in heme sites, the non-heme active sites have additional, exchangeable positions and provide new coordination modes for substrate and oxygen activation.[17] These enzymes can convert dioxygen to highly specialized reagents and catalyze the synthesis of many important biomolecules in aerobic organisms.[18,19] The biosynthesis of penicillin-type antibiotics[20,21] is a typical example among them.

Hydroxyethylphosphonate dioxygenase (HEPD) catalyzes a critical step in the phosphinothricin (PT) biosynthetic pathway (Scheme 1) as investigated in some genetic and biochemical experiments.[22–24] Synthetic PT is used in broad-spectrum agricultural herbicides for its bactericidal, fungicidal, and herbicidal properties.[22,25,26] HEPD activates O_2 by the divalent iron and catalyzes the conversion of 2-hydroxyethylphosphonate (2-HEP) to hydroxymethylphosphonate (HMP). This reaction would break a carbon–carbon single bond without any organic cofactor.[27]

Recently, the three-dimensional structure of HEPD has been crystallized in complexation with 2-HEP (Fig. 1). The crystal structure and relevant biochemical experiments provide much valuable information for the understanding of the catalytic mechanism of HEPD. However, both hydroperoxylation and

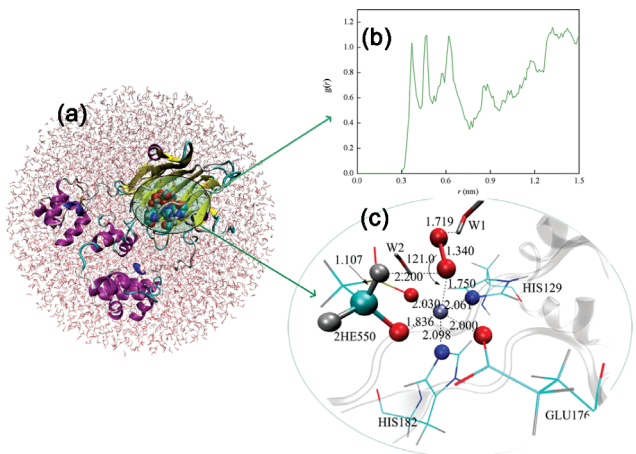

Fig. 1 (a) Schematic representation of the equilibrated model used in the subsequent QM and QM/MM calculation. The active site (also the QM region) is highlighted. (b) Radial distribution functions (RDFs) of water around the iron atom. The oxygen atom of water is used in calculation, and bin width of the center–center distance is 0.01 nm. (c) Optimized structures (the QM region) of the initial species with selected geometrical parameters obtained in QM/MM calculations (displayed with a ball and stick model).

Key Lab of Colloid and Interface Chemistry, Ministry of Education, Institute of Theoretical Chemistry, Shandong University, Jinan, 250100, P. R. China. E-mail: gaojun@sdu.edu.cn, cbliu@sdu.edu.cn; Fax: +86-531-88564464; Tel: +86-531-88363967 (J. G.); Tel: +86-531-88361398 (C. L.)

† Electronic supplementary information (ESI) available. See DOI: 10.1039/c1ob06221b

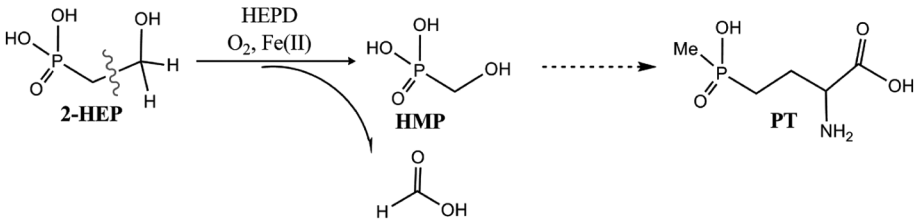

Scheme 1 HEPD catalyzes the conversion of 2-hydroxyethylphosphonate (2-HEP) to hydroxymethylphosphonate (HMP) during phosphinothricin (PT) biosynthesis.

hydroxylation mechanisms cannot provide a comprehensive interpretation for the experimental evidences.[27,28] Based on the cluster model of HEPD, the theoretical calculations at the DFT level suggest that both mechanisms are acceptable.[29] Much valuable information was provided in their calculations, such as the multiple reaction pathways. However, the active site of iron enzymes usually has a few low-lying spin states, and shows two state activities.[30–32] Their calculation did not consider the singlet spin state. And, the singlet state may also be very important to the catalytic reaction. At the same time, the flexibility of the active site cannot be considered in their model, such as the contributions of the secondary active site residues and trapped water. These conditions may strongly affect the catalytic process. For instance, the phosphonate oxygen atoms can be blocked from taking part in the reaction by the hydrogen bonds only in the presence of water molecules. The intermediate species can be interpreted only when oxygen derives from O_2 in exchange with water.[27]

In order to understand the relevant biochemical experimental facts,[27,28] we performed a series of *ab initio* hybrid quantum mechanics/molecular mechanics (QM/MM) calculations. A tunable catalytic mechanism of HEPD has been proposed based on QM/MM calculations. Three bifurcations of the catalytic cycle make the mechanism agree well with the seemingly contradicting experimental facts. The contributions of water and the environment are significant for the catalytic process. At the same time, theoretical studies on the flexibility of the active site may shed light on the development of more efficient catalysts.

2. Computational details

The theoretical model (Fig. 1a) was set up based on the X-ray crystal structure of HEPD in complexation with the substrate 2-HEP (PDB ID: 3GBF).[27] The protonation states of ionizable amino acids were selected and checked based on a visual inspection of their microenvironments. In the active site, the protonation states of His_{129} and His_{182} were kept in a neutral state, and the Glu_{176} was deprotonated. Although it seems to be natural to form a hydrogen bond with the hydroxyl oxygen and the nearby carboxylate oxygen of Glu_{176}, we noticed that the H-abstraction barrier was much lower with a deprotonated carboxyl group. This conclusion is very consistent with the previous theoretical calculations of Hirao *et al*.[29] And the deprotonated carboxyl group (serving as a general base) would facilitate the carbon–carbon bond cleavage (see Results and discussion section). Thus the deprotonated carboxyl group in Glu_{176} was adopted.

The classical molecular dynamic (MD) simulation with CHARMM22 force field[33] was performed and extended to 20 ns under stochastic boundary conditions [34] in the canonical (NVT) ensemble. Mean-square displacement (MSD) was adopted to depict the diffusive behaviour of the system (Fig. S1†). As shown in Fig. 1b, the distribution of water molecules around the active site was characterized by the radial distribution function (RDF). The coordination numbers for the first and the second solvent shells were about 2 and 4. Based on the result of RDF in MD simulation, two water molecules were included in the QM region. Only one or two water molecules may take part in the catalytic reaction directly, although more may affect the reaction (*via* cooperative water networks).[35–37] Thus the QM model is sufficient to interpret the carbon–carbon bond cleavage in HEPD. The spatial distribution function (SDF) gave further information on the possible location of water around the active site in three-dimensional space (Fig. S2†). The distribution density of water near the active site is mainly concentrated around O_2 and the substrate 2-HEP, which may be important in the catalytic reaction.[38] The snapshot of the equilibrated MD trajectory was taken as the starting point for further QM and QM/MM simulations.

The QM/MM computations were done using the ChemShell[39] package integrated with the Turbomole[40] and DL-POLY[41] programs. And the CHARMM22 force field[33] was used for the treatment of the MM part of the system. The electronic embedding scheme and the hydrogen link atoms with the charge shift model[42] for the QM/MM boundary were adopted in the QM/MM treatment. The 2-His-1-Glu facial triad (His_{129}, His_{182}, Glu_{176}), HEP, O_2, and two water molecules were included in the QM region with a total charge of –1. During the QM/MM geometry optimizations, the QM region and 7813 MM atoms (defined by including the residues within 20 Å of the QM region) were allowed to move, whereas all the remaining atoms were kept fixed as the environment. Two basis sets were employed in this study: B1 [Watcher+f [8s6p4d1f] (Fe)/6-31+G* (the coordinated atoms and the oxygen molecule)/6-31G** (rest)] was used for geometry optimizations, and B2 [Watcher+f (Fe)/6-31++G** (rest)] only served for single point calculations.[43,44] The Wachters basis set is a double-ζ quality with polarization functions on all atoms which have been used in iron-containing enzymes, such as myoglobin.[44] The GGA functional PBE was selected to be used throughout this work for all intermediates and transition state calculations. However, since there is no absolutely convincing reason to prefer this functional to the others, single point calculations were also performed to validate the PBE results with using B-P, B-LYP, PBE0 and B3LYP functionals as implemented in TURBOMOLE when the optimizations were done with PBE. A two-point displacement method with analytical calculations of gradients has been used to obtain the numeric frequency,[39] and the electronic polarization of the environment was included in the frequency calculation. Detailed analyses of the QM/MM system setup, MD

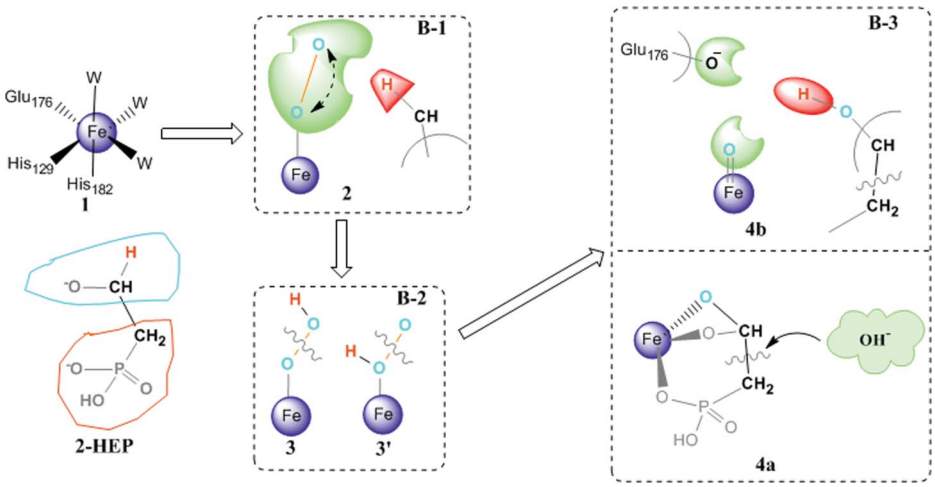

Scheme 2 Key character of suggested mechanism in the catalytic cycle of HEPD; the hydrogen atom abstraction, O–O bond cleavage and possible C–C bond cleavage steps were shown; **B-1**, **B-2**, **B-3** refer to different bifurcations in the reaction pathways. 2-HEP is the initial substrate.

simulation and the validation of the functionals are summarized in the supporting information.†

3. Results and discussion

3.1 Reaction mechanism in the catalytic cycle of HEPD

As shown in Scheme 2 and Scheme S1,† the catalytic cycle of dioxygen activation and carbon–carbon cleavage reactions has been well established by QM/MM calculations. This reaction mechanism agrees well with experimental evidences, *i.e.* the existence of an intermediacy derived from oxygen molecules. And the proton-assisted mechanism is supported in the catalysis reaction of HEPD.[27,45] The catalytic cycle starts at the resting state **1**, which has been characterized in the crystal structure.[27] Then O_2 molecules are bound with the open coordination position on the Fe^{II} to yield a reactive ferric superoxo species (Fe^{III}–[O_2^-], **2**). This is a general mechanistic strategy in several non-heme iron enzymes, such as hPheOH and PAH.[17,46–48] These steps are suggested to be relatively slow and thus biochemical studies have revealed various evidences and spectroscopic information.[17,49] However, the subsequent reduction of species **2** involves some intermediates which are short-lived, and thus are difficult to trap and characterize in experiments.

In the proposed mechanism, there are a few reaction pathways (three concatenated bifurcations) connecting the reactant and product. The first bifurcation (**B-1**) is related to a proton/electron transfer process, and in this step, the Fe^{III}–[O_2^-] species **2** is considered to attract a hydrogen atom from the CB atom of 2-HEP.[27,45] And the proton can switch to react with the distal or proximal oxygen atom to yield a hydroperoxo species (**3** or **3′**). This proton transfer step is the rate-limiting step as indicated in Scheme S1.† Later, the hydroperoxo species (**3** and **3′**) have a number of possible fates, such as the conversion of the bidentate substrate **3** to a tridentate complex **4a**, a hemiacetal **4b**, or a hydrogen bonded inverted metastable hydroperoxide [FeO···(HO)] species **4′**.[50,51] The flexible conversions may provide feedback regulation between first and second bifurcations. After the breaking of the O–O bond, the generated intermediates appear to be tunable by the pH conditions (**B-2**). The last bifurcation is a branch (derived from species **4b**) within the second one, and a proton-shuttle based mechanism is utilized to facilitate the carbon–carbon bond cleavage. Finally, the formate and HMP are generated. For the product state **5**, the coordinated formate releases firstly in the presence of water. And later it releases HMP and returns to its resting state **1**.

3.2 Properties of the ferric–superoxide intermediates

At the beginning, the O_2 molecules are bound with the Fe^{II} to yield a reactive ferric superoxo species (Fe^{III}–[O_2^-], **2**) as shown in Scheme 3. The ferric–superoxide species were optimized in the gas phase and QM/MM model. It suggested that the end-on geometry was preferred in the enzyme environment.[52] The environment seems to slightly lengthen the O–O bond distances (by 0.02 Å). The O–O bond length (1.3 Å) in this species is similar to the usual superoxide.[53] The environment alone is not sufficient for breaking the O–O bond. Table S2† gives the selected parameters of the optimized structure in the gas phase with different functionals for the cluster model. The GGA and *meta*-GGA functionals suggested a slightly tightly binding structure which was similar to the MP2 result, while the hybrid functionals provided the opposite trends.

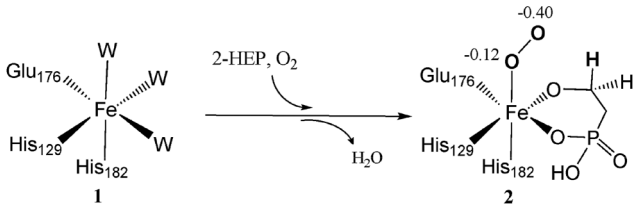

Scheme 3 The formation of the reactive ferric superoxo species (Fe^{III}–[O_2^-], **2**); The NPA charges of the distal and proximal oxygen atom were given.

The NPA partial charge was used to generate an intuitive and localized representation of the electron density. The iron in the active site is supposed to have a formal charge of +3, but a significant charge transfer from the ligands to metal can be

observed in the model. The NPA charge indicates a positive partial charge of 1.02e on the iron atoms. The distal oxygen atom (–0.40e) is more negative than the proximal oxygen atom (–0.12e). The total charge of O_2 is –0.52e suggesting that the negative charge of the whole system should be mainly concentrated on O_2 and partially transports to the iron.

3.3 The distal and proximal pathways in hydrogen-abstraction reaction

The hydrogen-attraction from the substrate occurs in the first bifurcation (**B-1**, Scheme 2). After the donor ligand (2-HEP) and O_2 bind to the 2-His-1-Glu facial, the hydrogen of 2-HEP will migrate to one oxygen atom of O_2. There are two potential choices: distal and proximal. Like the processes in Cytochrome P450,[54,55] the direction of the proton transfer process will be driven to different hydroperoxo intermediates (**3** or **3′**, Scheme 1).[27,45]

In Fig. 2 and Fig. S3,† the key optimized structures are displayed. The Fe–O bond is much stronger than the O–O bond and the optimized Fe–O–O angle is about 120°, which is in agreement with the results of similar low-spin Fe^{III}–OOH species.[11] Near the reaction centre, one water molecule (donated as **W1**) can form a strong hydrogen bond with the distal oxygen atom. And, for the transition state of the distal species, this water molecule involves in the vibration mode of the only imaginary frequency. Thus this water molecule may play an important role in the reaction. Another water molecule shows weaker contributions to this process, although it also forms a hydrogen bond with the substrate. The NPA partial charge suggests one-electron transport from the substrate to the Fe–O_2 motif in the proton transfer process.

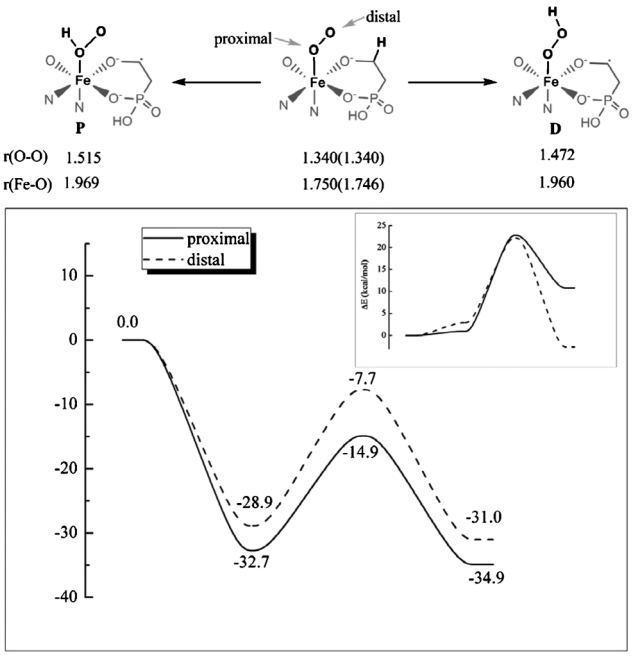

Fig. 2 Character of the hydrogen transfer process (identified as distal (**3**) and proximal (**3′**) species) and the relative energy profile (in kcal mol^{-1}) in QM/MM calculations and gas phase calculations (inset panel); the parameter for different initial configurations (species **2**, upper panel) was given. And the values are related to the distal and proximal (in the brackets) process; the zero point related to the energy of the initial optimized structure in our model. The first minima refer to the reactant.

Fig. 2 depicts the character of the hydrogen transfer process, and also the relative energy profile. The protonation of the oxygen atom of O_2 results in the significant weakening of the Fe–O and O–O bonds. In the product states, the elongation of the O–O and Fe–O bonds in the proximal species (by 0.22 and 0.28 Å) is a little larger than that in the distal species (by 0.21 and 0.13 Å). The activation barriers of the proximal and distal species are 17.8 and 21.2 kcal mol^{-1}, which is the rate-limiting step as indicated in Scheme S1.†

In this step, the highest energy barriers are obtained from BLYP (19.7 and 23.0 kcal mol^{-1}), and two hybrid functionals give relatively lower barriers, *i.e.* 12.7 and 17.9 kcal mol^{-1} for B3LYP (Table S3†). All these results indicate that the energy barrier is slightly lower for the proximal species. As the hybrid functionals gave a lower energy barrier than the GGA functionals, one may suggest that the energy barrier of the H-abstraction step was lower than the result of Hirao *et al*.[29] Single point calculations are also performed by way of removing the MM environments, and the energy barriers became 21.8 kcal mol^{-1} and 19.3 kcal mol^{-1} for the proximal and distal species. However, in this condition, the relative energy of the proximal isomer is higher than the distal species (by 13.4 kcal mol^{-1}). This implies that the proximal protonated product can easily go back to the reactant state since the barrier from the product to the reactant is much lower (about 12 kcal mol^{-1}). In the energy profile of Fig. 2, the zero point of energy is the energy of the initial optimized structure of the QM/MM model. The first minimum is the reactant. The difference between the initial structure and the reactant is the hydrogen bonds formed by water with the oxygen molecule and the substrate (Fig. S3†). The environment plays an important role in stabilizing the reactant and facilitating the following reaction. Interestingly, the proton affinities of ferric–superoxide species show significant environment dependence. The proximal isomer is preferred at the existence of the protein environment, while the distal isomer is more favourable in the gas phase. The fact that the distal species is favoured in the gas phase is also consistent with Cytochrome P450.[55] Furthermore, the proton can reside on both oxygen atoms, and the position of the proton can be discriminated by IR spectra. The predicted IR spectra of the O–O bond stretching give 737 cm^{-1} and 801 cm^{-1} for the proximal and distal species.

The barrier (19.3 kcal mol^{-1}) of the distal hydrogen attraction pathway is still much lower than the barrier obtained by Hirao *et al*.[29] The possible reasons are given here. First, our model and that of Hirao *et al.* were different. In the model of Hirao *et al.*, the 2-HEP was protonated, while ours was deprotonated. Our calculations suggested that the deprotonated substrate 2-HEP provided a lower energy barrier, and the protonated one gave a higher energy barrier. And Hirao *et al.*'s results also indicated a lower energy barrier (18.1 kcal mol^{-1}, similar to our 19.3 kal mol^{-1}) with the deprotonated substrate. However, they chose to assume that the substrate was protonated, which was deemed natural as they suggested.[29] However, maybe it is natural to assume the protonated substrate, this argument was not sufficient to deny the deprotonated substrate with a lower energy barrier. Furthermore, the absence of the proton between the hydroxyl oxygen and the nearby carboxylate oxygen of Glu_{176} would facilitate the carbon–carbon bond cleavage process (mechanism **b′**). If the 2-HEP is protonated, this mechanism would be blocked, and the energy barrier of the whole reaction would be higher than 30 kcal mol^{-1}.

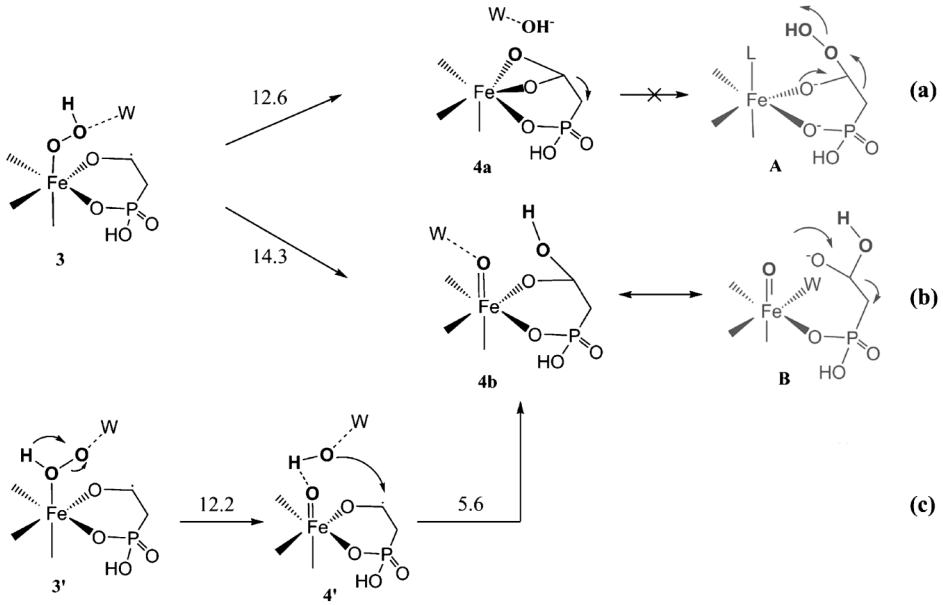

Scheme 4 The possible fates of the hydroperoxo species **3** and **3′**; the O–O bond cleavage happened in these reaction pathways; the species **A** and **B** with a gray color are the putative species proposed in experiments. The number above the arrow refers to the related energy barrier (in kcal mol^{-1}).

Second, both our QM and QM/MM models were based on the result of the molecular dynamic simulations, while Hirao *et al.*'s model was obtained directly from the crystal structure. And the flexibility of our model may cause the deviation. Third, the method (such as functional and basis sets) may also contribute to the differences.

3.4 The hydroperoxide species and the strength of O–O and Fe–O bond

The hydrogen transfer process results in the formation of the hydroperoxide species (**3** and **3′**, Fig. 2). The hydroperoxo species (**3** and **3′**) have a number of possible fates[56] as shown in Scheme 4 and Fig. S4.† The bifurcation of the hydroperoxylation and hydroxylation mechanisms largely relies on the uncertainty about the strength of the O–O and Fe–O bonds. Herein, these hydroperoxide species were used to examine the strength of the O–O and Fe–O bonds. Our results suggest a weaker O–O bond, and a much stronger Fe–O bond.

The optimized geometries in Scheme 4a show that the substrate converts from a bidentate species (**3**) to a tridentate species (**4a**). In this process, the O–O bond was broken simultaneously when the –OOH group migrated to the CB atom of 2-HEP. One water molecule was inserted into two oxygen atoms of O_2, and bridged the O_p atom and O_dH group. Then the O_dH group (with a NPA partial charge of –0.5e) underwent exchange with water molecules, and had the possibility to produce an O_wH group containing the oxygen from the water.[27] Along with the migration of the –OOH group the alternative electron transport from the substrate to the oxygen atoms of O_2. The NPA partial charge of O_2 became more negative (by 0.93e) in this step. We noted that the formation of the products was a strong exothermic reaction and thermodynamically favored in the QM/MM model. As labelled in Scheme S1,† an energy barrier of 12.6 kcal mol^{-1} was observed. This mechanism is different from the putative hydroperoxylation mechanism (**A**, Scheme 4), in which the Fe–O_p bond was assumed to break and the –OOH group would migrate to the CB atom followed by a Criegee rearrangement to break the carbon–carbon bond.

For the reaction path corresponding to Scheme 4b, the distal species **3** involves an initial O–O bond cleavage and the migration of the –OH group to the CB atom in 2-HEP to yield the species (Fe^{IV}=O, **4b**). The issues of dissociation of the O–O bond in the Fe^{III}–OOH moiety have been discussed for a number of heme and non-heme systems.[11,54,57,58] The corresponding optimized geometric structures were shown in Scheme 4b and Fig. S4.† In the structure of the reactant, a hydrogen bond (1.70 Å) formed between a water molecule (**W**, in Scheme 4) and an O_p atom, which slightly elongated the bond length of the Fe–O and O–O bonds in **R**. This may make the cleavage of the O–O bond easier since the length of O–O bond is similar to the O–O bond of H_2O_2. The NPA partial charges of O_p and O_d are similar in the reactant **R** (–0.49e and 0.50e). The computed energy barrier for the cleavage of the O–O bond and the formation of the CB–O_d bond was 14.3 kcal mol^{-1}, which is very close to the hemolytic O–O bond cleavage barrier of $P450_{cam}$.[59]

Most of the previously proposed mechanisms were restricted by the distal protonated species (**3**, in Scheme 4), which could comprehensively explain most of the experiment facts.[27,28] However, the proximal species (**3′**, Scheme 4) was also an energetic preferred species. Scheme 4c shows the fate of this proximal protonated hydorperoxo species (**3′**, Fe^{III}–(OH)–O). In the proposed mechanism, the proton transfers from the proximal oxygen atom to the distal one, and, at the same time, the O–O bond is broken. An inverted hydrogen bonded metastable hydroperoxide species (**4′**, [FeO···(HO)]) was then generated. The energy barrier of this reaction is 12.2 kcal mol^{-1}. The Fe–O_p bond is strengthened (1.647 Å) and the distance between the iron and nitrogen of His_{182} is also shortened by 0.14 Å. This moiety has also been proposed in the mono-oxygenases.[38,39,59] The metastable intermediate can

easily yield the species **4b** with an energy barrier of 5.6 kcal mol^{-1}. The NPA partial charge on the CB atom of the substrate was 0.1e positive, which rendered it easier to be attacked by an OH group in a later step.

The O–O bond is weaker than the Fe–O bond for both distal protonated species (**3**, Fe^{III}–OOH) and proximal species (**3′**, Fe^{III}–(OH)–O). The normal mode analysis suggests the frequencies relevant to Fe–O and O–O bond be 510 and 801 cm^{-1} for the distal protonated species (**3**, Fe^{III}–OOH), while the frequencies are 519 and 737 cm^{-1} for the proximal species (**3′**, Fe^{III}–(OH)–O). The O–O bond would break in advance. This is consistent with the activated bleomycin (ABLM) or the Fe^{III}–alkylperoxo models.[60–62] This effect may stem from the electronic structure description.[11] In a low-spin complex, the unoccupied d orbitals allow strong σ donation from σ-bonding and π-bonding orbitals on this hydroperoxide, which will strengthen the peroxide–iron bond and weaken the O–O bond. So the low-spin hydroperoxo species is active for the cleavage of the O–O bond. In this process, the role of the trapped water in the active site was proposed to strengthen the catalytic ability of the enzyme, and improve the transition state stabilization.[63]

3.5 Reaction mechanism of carbon–carbon bond cleavage

The details of three types of carbon–carbon bond cleavage mechanisms were illustrated in Scheme 5. The carbon–carbon bond cleavage reaction initializes from a tridentate species or a hemiacetal species derived from the bidentate substrate. Then, the carbon–carbon single bond of the substrate would break directly. The loss of stereochemistry in the catalytic process of HEPD can be well interpreted in this mechanism.[64]

In the presence of a tridentate species (**4a-1**) and the hydroxyl ion group (OH$^-$), the carbon–carbon bond would break easily with an energy barrier of 16.9 kcal mol^{-1} (Scheme 5). Then, the hydroxyl ion group (OH$^-$) would attack the CA atom to yield HMP with a negligible energy barrier (**4a-2**). The energy barrier is very low (about 1.0 kcal mol^{-1}). Because the generation of the final product is very exothermic (about 40 kcal mol^{-1}), HMP and formate could generate in a very fast fashion. The corresponding optimized structures in Fig. S5† suggested that the water molecule is also important.

It is a stepwise mechanism for the broken of carbon–carbon bond would occur after the formation of the CA–OH bond. One may suggest that the breaking of the carbon–carbon bond and the formation of the CA–OH bond occur simultaneously. However, this concerted mechanism has been excluded. We did try various potential energy surface (PES) scans by restraining relevant internal coordinates, but only the stepwise mechanism was obtained. Only after the carbon–carbon bond cleavage could the formation of the CA–OH bond occur to yield HMP. The charge distributions of the product are more dispersed than the reactants.

The putative hydroperoxylation mechanism suggests that a Criegee-type rearrangement (**A**, Scheme 4) may occur to yield O-formyl-HMP (OFHMP).[27,28] However, the rearrangement is hard to happen due to the stability of the tridentate ligand (species **4a**), in which the distal oxygen atom would still bind to the iron after the migration of the –OOH group. The Criegee-type rearrangement mechanism has been examined by restraint energy scans. The energy barrier is too high (larger than 60 kcal mol^{-1}) for an enzymatic reaction. This conclusion was similar to a previously proposed mechanism, although very different models were adopted.[29] This might also explain the experimental fact that O-formyl-HMP (OFHMP) could not be accepted as a substrate.[28]

The third bifurcation (**B-3**, Scheme 5) is related to the carbon–carbon bond cleavage reaction *via* a proton-shuttle mechanism (paths **b** and **b′**, Scheme 5). The key characters of this reaction are

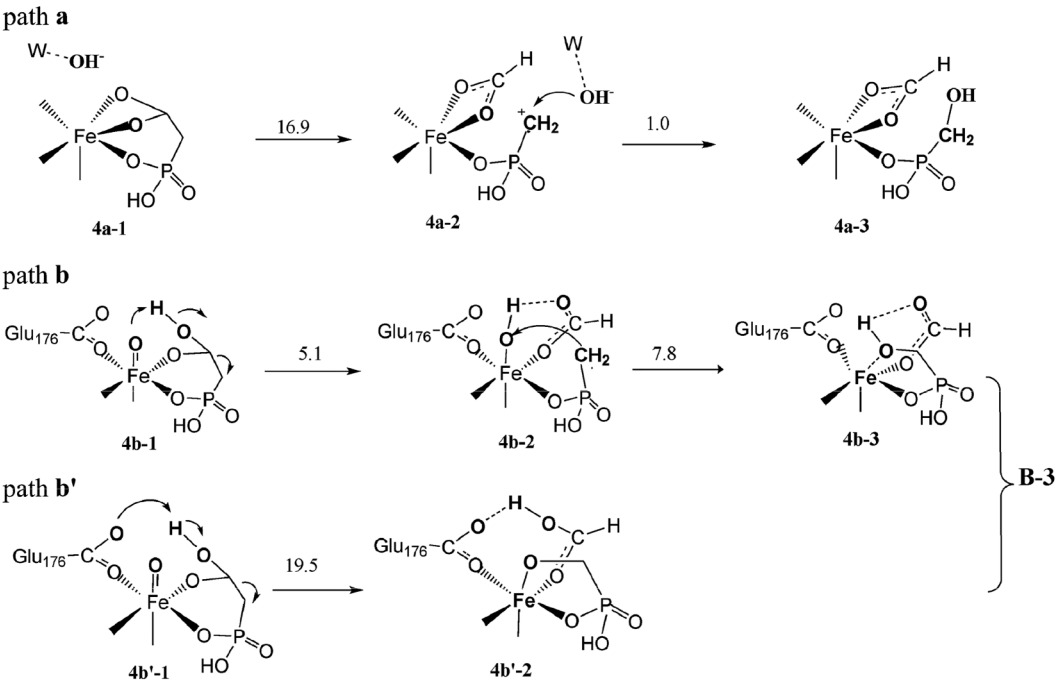

Scheme 5 The possible reaction pathways in the carbon–carbon bond cleavage; the species **4b-1** and **4b′-1** are similar complexes which have different configurations. The numbers above the arrow refer to the related energy barrier (in kcal mol^{-1}).

shown in Scheme 5. And the proton transfer process is crucial to break the carbon–carbon bond. As the elongation of the carbon–carbon bond in path **b**, the hydrogen atom of the CB–OH group in the substrate would shift to the oxygen atom of the Fe–O group in a concerted mechanism (**4b-1**, Scheme 5). Later, the CH_2 group in the substrate would rotate and bond to the oxygen atom in the Fe–OH group. After the rotation of the CH_2 group, a resonance-stabilized anion species (**4b-2**, Scheme 5) was obtained to yield HMP. Interestingly, the proton might shuttle back to the newly generated formate, which was the so-called ping-pong kinetics. Our calculations indicate that a stepwise mechanism is favoured. The cleavage of the carbon–carbon bond would occur firstly, followed by the rotation of the CH_2 group to yield the final products. This mechanism has been confirmed by PES scans. The corresponding optimized structures are also given in Fig. S5.† The hydrogen bond between one oxygen atom in the substrate and the Fe–OH group becomes stronger (1.330 Å) after the formation of the resonance-stabilized anion species. This mechanism is similar to the putative hydroxylation mechanism (**B**, Scheme 4), except that no water molecule is bound with the iron atom in species **4b**.

In path **b′**, the catalytic role of the carboxyl group in residue Glu_{176} is considered. The optimized structures are given in Fig. S5.† If the O–H bond in the substrate rotates to the direction toward the carboxyl group of Glu_{176}, the proton could also migrate to the non-coordinated oxygen atom in residue Glu_{176}. The carbon–carbon single bond would break simultaneously. After this step, a resonance-stabilized anion species (**4b′-2**, Scheme 5) would generate without any energy barrier. In the simulations, if the above O–H bond in the reactant (**R**, Fig. S5†) was restrained, the energy scan profile along the distance of the carbon–carbon bond should be simply uphill, no stable intermediates could be located, and then the unconstrained optimization would lead back to the reactant. Therefore, the breaking of the carbon–carbon bond and the rotation of the CH_2 group are done in a concerted mechanism, which is different from the previous pathways (path **a**, **b**).

The proton transfer and the carbon–carbon bond cleavage step should occur in a concerted step in path **b** and **b′**. At the same time, the breaking of the carbon–carbon bond also contributes to the proton transfer process. An energy scan has been performed by way of pulling the proton to the Fe^{IV}=O group or Glu_{176}. By applying such judicious constraints, one may obtain the formation of the O–H bond while the carbon–carbon bond is retained. But the corresponding energy profile is simply uphill, and reaches a plateau (about 6.0 kcal mol^{-1}). Later, the unconstrained optimization of such species along this path would not yield any local minima, but would lead back to the reactant directly. Thus we could conclude that the proton transfer and the carbon–carbon bond cleavage step should occur in a concerted step.

The energy barriers of the proton-shuttle based mechanisms (**b** and **b′**) are 5.1 and 19.5 kcal mol^{-1} (Fig. 3). But the energy barrier related to the rotation of the CH_2 group was a little higher (7.8 kcal mol^{-1}) in path **b**, while the mechanism in path **b′** requires no additional steps to complete the carbon–carbon bond cleavage reaction. It is notable that the residue Glu_{176} is not as uninvolved as the two His residues. It also contributes to tune the activity of the enzyme by modulating its protonated states. This idea may be suggestive for enzyme mutation and designing experiments to explore why the HEPD enzyme contains a 2-His-1-carboxylate motif rather than a 3-His motif. In general, the residue Glu_{176} or

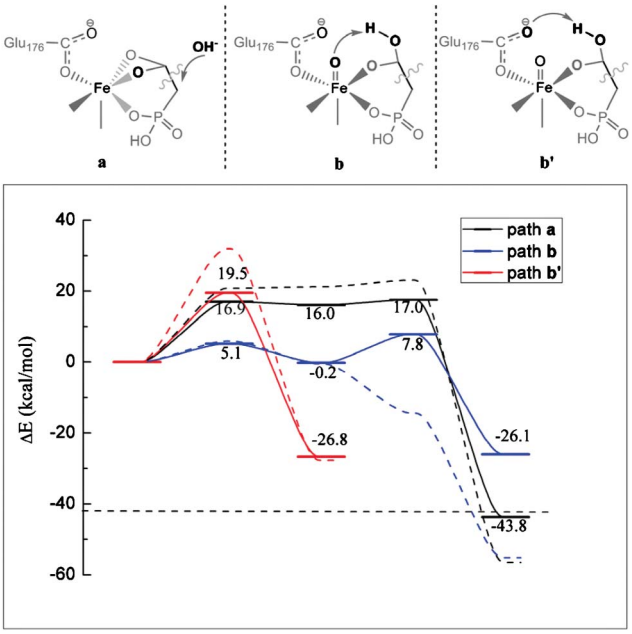

Fig. 3 The key characters (upper panel) and calculated energy profiles (bottom panel, kcal mol^{-1}) in the carbon–carbon bond cleavage process; three pathways are shown, identified as **a**, **b** and **b′**; in the energy profile, QM/MM calculations (solid curve) and gas phase calculations (dash curve) are also given; the straight dash line in the plot indicates the relative energy of the species (**5**, Scheme S1).

the Fe^{IV}=O group would serve as a general base to accept a proton and facilitate the carbon–carbon bond cleavage.

3.6 The critical role of enzyme environment

The polarization of the active site by the environment is an important issue in an enzyme model. We have calculated the dipole and quadruple to indicate the effect of the polarization. The dipole of the QM region including the point charge of the protein environment was 963.0 Debye, and reduced to 79.4 Debye in the gas phase. The anisotropy constant of quadruple increased about 56 times when the MM environment was considered. How does the environment contribute to the electronic polarization in the QM region? The electron density maps are suggested as a sensitive tool for investigating the global rearrangement of electrons.[65–67] Here, the total electron density differences were visualized to account for charge polarization in the QM region (Fig. 4). The environment strongly affects the electron density distribution. The hydrogen on the CB atom of HEP is more positive (green), which makes it easier to attract the more negative (yellow) oxygen atom in oxygen molecule. The oxygen atoms in the carboxyl group of Glu_{176} show a different trend, and the coordinated oxygen atom is more positive while the other one in the carboxyl is more negative. The water molecule in the QM region is also polarized, which makes the hydrogen atom more electrophilic. The NPA partial charge analysis indicated that oxygen atoms are more negative (by 0.08e), while hydrogen atoms are more positive (by 0.05e).

The electronic density difference distribution of the QM region may be interpreted by the hydrogen bond interactions. One can find that the non-coordinated oxygen atom in carboxyl group of Glu_{176} could form hydrogen bonds (1.69 and 1.70 Å) with

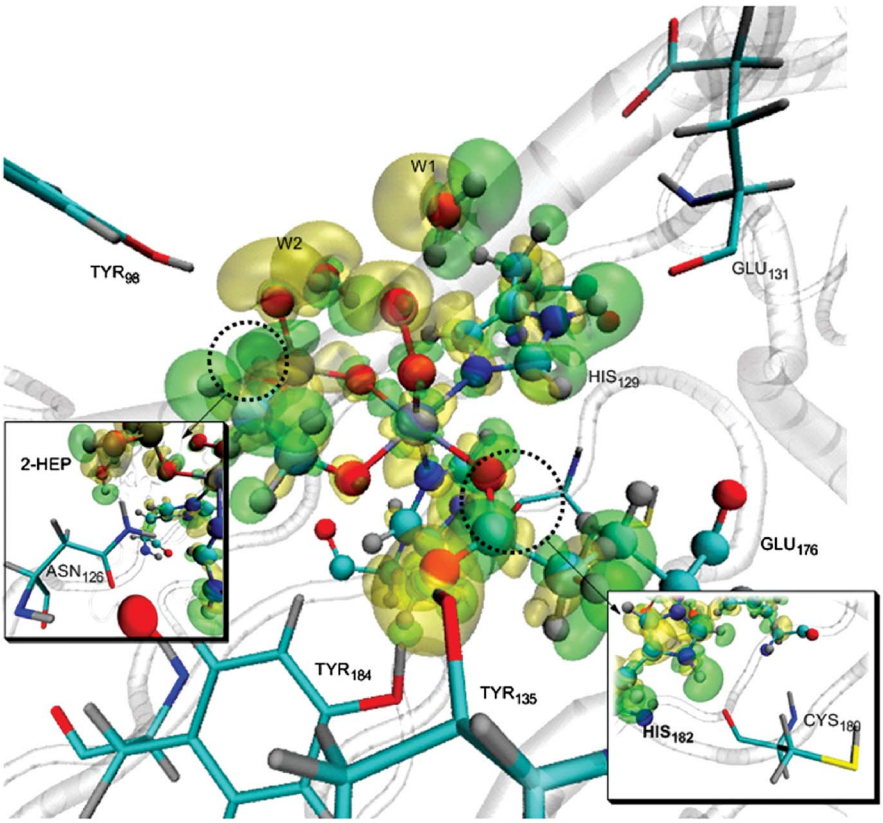

Fig. 4 Total electron density difference map between QM/MM and QM calculation (isovalue: –0.001 for green, and 0.001 for yellow).

Tyr_{184} and Thr_{135}. The oxygen atoms of residue Glu_{131} and Cys_{180} (accepters) can form hydrogen bonds interacted with His_{129} and His_{180} (donors). The cation–π interaction [68–71] may also contribute to the electronic density difference in the aromatic ring of both histidines. Several water molecules also form the hydrogen bond with the substrate and oxygen molecule. In most cases, hydrogen bond interactions are found to be the crucial factors to the region of the increase and decrease of electronic density. The structure obtained from the QM/MM optimization was compared with the crystal structure. A hydrogen bond interaction between Tyr_{98} and one of the phosphonate oxygen atoms of HEP was observed as mentioned in the crystal structure.[27] The donor and acceptor distance of another hydrogen bond between N2(Asn_{126}) and O1(2-HEP) is 2.89 Å (2.83 Å in the crystal structure).

We also visualized the total electron density differences of other intermediates, such as species **4a** and **4b** related to the carbon–carbon bond cleavage step (Fig. S7†). For **4a**, the electron density on the CA atom was more positive (green), while the charge on the O_d atom was more negative and polarized. For **4b**, the similar trends of electron density on the CA and O_p atoms were observed. The electron density on iron was also strongly polarized by the protein environment. Further work such as a computational enzyme mutation design would be required for a detailed illustration.

The six secondary active site residues, including Tyr_{98}, Asn_{126}, Tyr_{184}, Thr_{135}, Glu_{131} and Cys_{180} show strong effects on the active site *via* hydrogen bonding interactions. Given a relatively quantitative estimation, single point energy calculations were performed by way of eliminating the coulomb contribution of the relevant residues in the MM region. Electrostatic stabilization energy (ΔE) was defined as the difference between the total energy with the relevant residue and the energy without that relevant residue. And the energy contributions from these residues were illustrated in Fig. 5. The residue Glu_{131} seems to increase the relative energy of the system, while the contribution of others mainly lowers the energy while Asn_{126} provides the largest contribution. We may categorize the MM part into two regions: the local region which refers to the residues within 3 Å of the QM region and the global region which is defined as the region beyond the local region. The

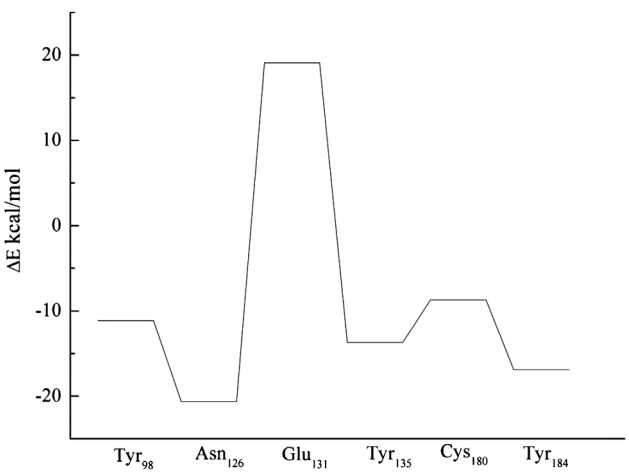

Fig. 5 Electrostatic stabilization energy (kcal mol^{-1}) from the secondary active-site residues.

sum of the electrostatic energy contributions from the local region was nearly 88%, including the protein residues (47%) and water (41%). Therefore, the secondary active site residues in enzymes and water molecules mainly contribute tothe catalytic environment, and define the electrostatic environment of the active site.

As for the nature of the substrate, the carbon–carbon bond dissociation energy of 2-HEP in the gas phase (without the active site) was calculated at the PBE/B2 level. And it was very high, *i.e.* more than 80 kcal mol^{-1}, which was consistent with the usual carbon–carbon single bond dissociation energy. In the same manner, the carbon–carbon bond dissociation energy of other intermediates, such as the species of **4a** and **4b**, was also calculated, and the energy barrier was still high (50~70 kcal mol^{-1}). Then, the energy scans to elongate the carbon–carbon bond distance of 2-HEP in the enzyme environment (without the incoming of O_2) made the profile reach a plateau (about 40 kcal mol^{-1}) when the carbon–carbon distance reached more than 3.0 Å.

The generated hydroxyl ion group (OH) can explain the experimental evidence that the oxygen atom of water could incorporate into HMP (path **a**, Scheme 5).[27] The energy barrier of the Criegee-type rearrangement mechanism was very high, and this could explain the experimental fact that O-formyl-HMP (OFHMP) could not be accepted as a substrate. In the process (**3**→**4a**), neither the other residues nor the water molecules would coordinate with the metal center, and instead a tridentate ligand would be yielded and sufficiently lower the relative energy of these species. Calculations indicated that, after the breaking of the carbon–carbon bond, the following steps were very exothermic, and thus most intermediates would have a very short lifetime. The energy barriers in all reaction channels are acceptable for an enzymatic reaction in the protein environment.

In order to consider the temperature effects on the stability of the local active site, we adopt the quantum mechanical/molecular mechanical (QM/MM) molecular dynamics (MD) simulation for 10 ps in an NVT ensemble (details in Table S4†). The results revealed that the deviation between the average structure parameters and the optimized ones was in the range of 0.1 Å. The temperature mainly affected the coordinated bond length, and the fluctuation of the O–O bond was relatively small (about 0.05 Å). However, the Fe–O–O angle would vary more than 10°, which led the O atom to be easier to approach the hydrogen atom in the substrate. Most of the hydrogen bond interactions in the secondary active site residues were preserved in the dynamic process. Several less mobile water molecules at the active site were observed. During the 10 ps *ab initio* QM/MM MD, no other significant change was observed.

3.7 Toward tuning of the carbon–carbon bond cleavage reaction

As in Scheme 5 and Fig. S5,† the presence of water and OH in the active sites strongly affects the reaction pathways. The substrate in species **4a** may accept the hydroxyl ion (OH^-), while in the species **4b**, the substrate would provide the proton. Since the species **4a** needs an additional hydroxyl group (OH^-), the enrichment of OH^- results in more products from path **a**, and *vice versa*.[49] And the intermediates from the first bifurcation (H-attraction step) may be balanced *via* the second bifurcation. Furthermore, for species **4b**, the proton transfer can occur toward not only the oxygen atom of the Fe^{IV}═O group but also the oxygen atom of Glu_{176}. Thus, the regulation of the third bifurcation could make the protein robust to some degree. If some mutations change the protein environment and result in blocking one of the reaction pathways, another would still remain. However, when some factors change, such as the incoming substrate analogues, the regulation of the reaction pathway may lead to the yielding of by-products. The mutation of the environment around the reaction centre may offer a control of these bifurcations. For example, the strength of the electronic field may affect these chemical events (such as the H-attraction step) as in the example of Cytochrome P450.[72,73] In general, this is a flexible reaction mechanism which yields only one product.

Meanwhile, some reaction steps show uncontrollable character, even though they are environment-dependent. The protein environment seems to lower the relative energy barriers in the mechanism (see Fig. 3), which would accelerate the C–C bond cleavage reaction. With the protein environment, we may also obtain more stable intermediates. For instance, the intermediates **3** and **3b** are more stable in the protein environment. In path **a**, the energy barrier related to this C–C bond cleavage step is only 1.0 kcal mol^{-1} higher than that of the generated product. And the transition state disappears without the environment. In path **b**, the energy profiles of this proton-transfer based carbon–carbon bond cleavage are comparable with the results from gas phase calculations. But the second energy barrier related to the rotation of the CH_2 group vanishes, which suggests that this be an energy-preferred reaction in the gas phase. In path **b′**, the protein environment shows relatively fewer effects on the reaction mechanism, and only the energy barrier shifts higher. Additionally, we observed that the protein environment showed minor effects (1–2 kcal mol^{-1}) on the conversion of the hydroperoxo species (**3** or **3′**) to the species **4a** and **4b**.

4. Conclusion

In summary, a tunable reaction mechanism with three bifurcations was determined within the framework of *ab initio* QM/MM simulations. Further evidence was provided against the originally proposed catalytic mechanism. The effect of the secondary active site residues and the role of "trapped" water in the active site were illustrated. The complete reaction pathways and the corresponding energy barriers were determined. The energy barriers are considerably low (most below 20 kcal mol^{-1}). And the total energy barrier was lower than the results in the theoretical calculations of Hirao *et al*.[29] These results provide a nice interpretation of the seeming contradicting experimental evidence obtained through kinetic isotope effect studies and product distributions analysis.

The breaking of the carbon–carbon bond may be achieved through a tridentate binding ligand derived from the hydroperoxo species, or employ a proton-shuttle assisted mechanism, in which the concerted proton transfer process is essential to break this carbon–carbon bond. The reaction direction in the carbon–carbon bond cleavage seems to be tunable under different acid/base conditions. And this flexible catalytic ability of the enzyme may be formed in the evolution. In the first bifurcation, the proton can reside on either of the oxygen atoms of the ferric–superoxide species. It is the rate-determining step and the enzyme environment significantly affects the reaction barrier of both proton transfer processes. For the hydroperoxo species, the O–O bond would be broken in advance, while the Fe–O bond could be retained. In the

active site, the residue Glu_{176} also contributes to tune the activity of the enzyme by modulating its protonated state. It is suggested that the polarization by the local active sites should be important. Our calculations suggested that the trapped water in the active site strengthens the catalytic ability of the enzyme, and improves the transition state stabilization. This would provide additional flexibility in the multi-pathway reaction scenario. The enzyme environment can significantly lower the reaction barriers, and may be responsible for rendering the catalytic process mild – neither energy-demanding nor energy-wasting.

We note that these bifurcations in the reaction pathway can be regulated in the presence of water, hydroxyl ion group and mutation of the enzyme to some degree, which makes the enzyme more robust in evolution and the perturbation of the environment. Just like the reaction mechanism of the porphyrin molecule in heme sites,[74–78] the Boolean logic regulated reaction mechanism still exists in non-heme enzymes. The control of these logic operations is still an open issue. Further comprehensive studies were required to provide more electronic structure information to account for the effect of the protein environment. Mutation of the enzyme and alternative substrates are potential pathways for the control.

Acknowledgements

This work is supported by the National Natural Science Foundation of China (No. 20873075), Natural Science Foundation of Shandong Province of China (No. ZR2010BZ005) and Independent Innovation Foundation of Shandong University (2009JC018, 2010TS015). This work also supported by Virtual Laboratory for Computational Chemistry, Supercomputing Center of Chinese Academy of Science and High Performance Computing Center of Shandong University.

References

1 K. D. Koehntop, J. P. Emerson and L. Que, *JBIC, J. Biol. Inorg. Chem.*, 2005, **10**, 87–93.
2 M. Sono, M. P. Roach, E. D. Coulter and J. H. Dawson, *Chem. Rev.*, 1996, **96**, 2841–2888.
3 M. Costas, M. P. Mehn, M. P. Jensen and L. Que, *Chem. Rev.*, 2004, **104**, 939–986.
4 A. Ozer, R. K. Bruick and Nat, *Chem. Biol.*, 2007, **3**, 144–153.
5 A. De La Lande, D. R. Salahub, J. Maddaluno, A. Scemama, J. Pilme, O. Parisel, H. Gerard, M. Caffarel and J.-P. Piquemal, *J. Comput. Chem.*, 2011, **32**, 1178–1182.
6 A. Bassan, T. Borowski and P. E. M. Siegbahn, *Dalton Trans.*, 2004, 3153–3162.
7 M. Costas, M. P. Mehn, M. P. Jensen and L. Que, *Chem. Rev.*, 2004, **104**, 939–986.
8 A. Decker, J. U. Rohde, E. J. Klinker, S. D. Wong, L. Que and E. I. Solomon, *J. Am. Chem. Soc.*, 2007, **129**, 15983–15996.
9 J.-U. Rohde, M. R. Bukowski and L. Que, *Curr. Opin. Chem. Biol.*, 2003, **7**, 674–682.
10 A. J. Simaan, F. Banse, J.-J. Girerd, K. Wieghardt and E. Bill, *Inorg. Chem.*, 2001, **40**, 6538–6540.
11 E. I. Solomon, S. D. Wong, L. V. Liu, A. Decker and M. S. Chow, *Curr. Opin. Chem. Biol.*, 2009, **13**, 99–113.
12 A. Chanda, F. T. de Oliveira, T. J. Collins, E. Munck, E. L. Bominaar and Inorg, *Chem.*, 2008, **47**, 9372–9379.
13 D. Rinaldo, D. M. Philipp, S. J. Lippard, R. A. Friesner and J. Am. Chem, *Soc.*, 2007, **129**, 3135–3147.
14 P. C. A. Bruijnincx, G. van Koten and R. J. M. Klein Gebbink, *Chem. Soc. Rev.*, 2008, **37**, 2716–2744.
15 A. Decker and E. I. Solomon, *Curr. Opin. Chem. Biol.*, 2005, **9**, 152–163.
16 S. J. Friese, B. E. Kucera, L. Que and W. B. Tolman, *Inorg. Chem.*, 2006, **45**, 8003–8005.
17 E. I. Solomon, A. Decker and N. Lehnert, *Proc. Natl. Acad. Sci. U. S. A.*, 2003, **100**, 3589–3594.
18 D. T. Gibson and R. E. Parales, *Curr. Opin. Biotechnol.*, 2000, **11**, 236–243.
19 A. S. Hakemian and A. C. Rosenzweig, *Annu. Rev. Biochem.*, 2007, **76**, 223–241.
20 J. E. Baldwin and S. E. Abraham, *Nat. Prod. Rep.*, 1988, **5**, 129–145.
21 N. J. Kershaw, M. E. C. Caines, M. C. Sleeman and C. J. Schofield, *Chem. Commun.*, 2005, 4251–4263.
22 D. Schwartz, S. Berger, E. Heinzelmann, K. Muschko, K. Welzel and W. Wohlleben, *Appl. Environ. Microbiol.*, 2004, **70**, 7093–7102.
23 E. Bayer, K. H. Gugel, K. Hägele, H. Hagenmaier, S. Jessipow, W. A. König and H. Zähner, *Helv. Chim. Acta*, 1972, **55**, 224–239.
24 J. A. V. Blodgett, P. M. Thomas, G. Li, J. E. Velasquez, W. A. van der Donk, N. L. Kelleher and W. W. Metcalf, *Nat. Chem. Biol.*, 2007, **3**, 480–485.
25 A. Kim, J. Kim, B. M. Martin and D. Dunaway-Mariano, *J. Biol. Chem.*, 1998, **273**, 4443.
26 H. Seto and T. Kuzuyama, *Nat. Prod. Rep.*, 1999, **16**, 589.
27 R. M. Cicchillo, H. Zhang, J. A. V. Blodgett, J. T. Whitteck, G. Li, S. K. Nair, W. A. van der Donk and W. W. Metcalf, *Nature*, 2009, **459**, 871–874.
28 J. T. Whitteck, R. M. Cicchillo and W. A. v. d. Donk, *J. Am. Chem. Soc.*, 2009, **131**, 16225–16232.
29 H. Hirao and K. Morokuma, *J. Am. Chem. Soc.*, 2010, **132**, 17901–17909.
30 H. Hirao, D. Kumar, L. Que and S. Shaik, *J. Am. Chem. Soc.*, 2006, **128**, 8590–8606.
31 D. Kumar, W. Thiel and S. P. de Visser, *J. Am. Chem. Soc.*, 2011, **133**, 3869–3882.
32 T. Borowski and P. E. M. Siegbahn, *J. Am. Chem. Soc.*, 2006, **128**, 12941–12953.
33 D. Bashford, Bellott, R. L. Dunbrack, J. D. Evanseck, M. J. Field, S. Fischer, J. Gao, H. Guo, S. Ha, D. Joseph-McCarthy, L. Kuchnir, K. Kuczera, F. T. K. Lau, C. Mattos, S. Michnick, T. Ngo, D. T. Nguyen, B. Prodhom, W. E. Reiher, B. Roux, M. Schlenkrich, J. C. Smith, R. Stote, J. Straub, M. Watanabe, J. Wiorkiewicz-Kuczera, D. Yin and M. Karplus, *J. Phys. Chem. B*, 1998, **102**, 3586–3616.
34 C. L. B. III and M. Karplus, *J. Chem. Phys.*, 1983, **79**, 6312–6325.
35 B. de Courcy, L. G. Pedersen, O. Parisel, N. Gresh, B. Silvi, J. Pilmé and J. P. Piquemal, *J. Chem. Theory Comput.*, 2010, **6**, 1048–1063.
36 J. Bonin, C. Costentin, C. Louault, M. Robert and J.-M. Savéant, *J. Am. Chem. Soc.*, 2011, **133**, 6668–6674.
37 B. de Courcy, J.-P. Piquemal, C. Garbay and N. Gresh, *J. Am. Chem. Soc.*, 2010, **132**, 3312–3320.
38 Z. Cao, Y. Mo and W. Thiel, *Angew. Chem., Int. Ed.*, 2007, **46**, 6811–6815.
39 P. Sherwood, A. H. de Vries, M. F. Guest, G. Schreckenbach, C. R. A. Catlow, S. A. French, A. A. Sokol, S. T. Bromley, W. Thiel, A. J. Turner, S. Billeter, F. Terstegen, S. Thiel, J. Kendrick, S. C. Rogers, J. Casci, M. Watson, F. King and E. Karlsen, *J. MOL. STRUC-THEOCHEM*, 2003, **632**, 1–28.
40 R. Ahlrichs, M. Bär, M. Häser, H. Horn and C. Kölmel, *Chem. Phys. Lett.*, 1989, **162**, 165–169.
41 W. Smith and T. R. Forester, *J. Mol. Graphics*, 1996, **14**, 136–141.
42 D. Bakowies and W. Thiel, *J. Phys. Chem.*, 1996, **100**, 10580–10594.
43 A. J. H. Wachters, *J. Chem. Phys.*, 1970, **52**, 1033–1036.
44 H. Chen, M. Ikeda-Saito and S. Shaik, *J. Am. Chem. Soc.*, 2008, **130**, 14778–14790.
45 D. Balcells, E. Clot and O. Eisenstein, *Chem. Rev.*, **110**, 749–823.
46 O. Andreas Andersen, T. Flatmark and E. Hough, *J. Mol. Biol.*, 2002, **320**, 1095–1108.
47 E. I. Solomon, T. C. Brunold, M. I. Davis, J. N. Kemsley, S.-K. Lee, N. Lehnert, F. Neese, A. J. Skulan, Y.-S. Yang and J. Zhou, *Chem. Rev.*, 1999, **100**, 235–350.
48 E. C. Wasinger, N. Mitić, B. Hedman, J. Caradonna, E. I. Solomon and K. O. Hodgson, *Biochemistry*, 2002, **41**, 6211–6217.
49 S. de Visser, J. Valentine and W. Nam, *Angew. Chem., Int. Ed.*, 2010, **49**, 2099–2101.
50 R. D. Bach and O. Dmitrenko, *J. Am. Chem. Soc.*, 2006, **128**, 1474–1488.
51 R. D. Bach and O. Dmitrenko, *J. Org. Chem.*, 2010, **75**, 3705–3714.

52 J. Conradie, D. A. Quarless, H. F. Hsu, T. C. Harrop, S. J. Lippard, S. A. Koch and A. Ghosh, *J. Am. Chem. Soc.*, 2007, **129**, 10446–10456.
53 C. J. Cramer, W. B. Tolman, K. H. Theopold and A. L. Rheingold, *Proc. Natl. Acad. Sci. U. S. A.*, 2003, **100**, 3635–3640.
54 F. Ogliaro, S. P. de Visser, S. Cohen, P. K. Sharma and S. Shaik, *J. Am. Chem. Soc.*, 2002, **124**, 2806–2817.
55 D. L. Harris and G. H. Loew, *J. Am. Chem. Soc.*, 1998, **120**, 8941–8948.
56 B. Arianna, R. A. B. Margareta, E. M. S. Per and Q. Lawrence Jr., *Angew. Chem., Int. Ed.*, 2005, **44**, 2939–2941.
57 A. J. Allentoff, J. L. Bolton, A. Wilks, J. A. Thompson and P. R. Ortiz de Montellano, *J. Am. Chem. Soc.*, 1992, **114**, 9744–9749.
58 A. Bassan, M. R. A. Blomberg, P. E. M. Siegbahn and L. Que, *J. Am. Chem. Soc.*, 2002, **124**, 11056–11063.
59 J. Zheng, D. Wang, W. Thiel and S. Shaik, *J. Am. Chem. Soc.*, 2006, **128**, 13204–13215.
60 N. Lehnert, R. Y. N. Ho, L. Que and E. I. Solomon, *J. Am. Chem. Soc.*, 2001, **123**, 12802–12816.
61 N. Lehnert, R. Y. N. Ho, L. Que and E. I. Solomon, *J. Am. Chem. Soc.*, 2001, **123**, 8271–8290.
62 N. Lehnert, F. Neese, R. Y. N. Ho, L. Que and E. I. Solomon, *J. Am. Chem. Soc.*, 2002, **124**, 10810–10822.
63 M. Zhao, D. T. Song and S. J. Lippard, *Inorg. Chem.*, 2006, **45**, 6323–6330.
64 J. T. Whitteck, P. Malova, S. C. Peck, R. M. Cicchillo, F. Hammerschmidt and W. A. van der Donk, *J. Am. Chem. Soc.*, 2011, 4236–4239.
65 K. Senthilkumar, J. I. Mujika, K. E. Ranaghan, F. R. Manby, A. J. Mulholland and J. N. Harvey, *J. R. Soc. Interface*, 2008, **5**, 207–216.
66 F. Bartha, O. Kapuy, C. Kozmutza and C. Van Alsenoy, *J. MOL. STRUC-THEOCHEM*, 2003, **666–667**, 117–122.
67 N. Strickland, A. J. Mulholland and J. N. Harvey, *Biophys. J.*, 2006, **90**, L27–L29.
68 J. P. Gallivan and D. A. Dougherty, *Proc. Natl. Acad. Sci. U. S. A.*, 1999, **96**, 9459–9464.
69 D. Quiñonero, C. Garau, C. Rotger, A. Frontera, P. Ballester, A. Costa and P. M. Deyà, *Angew. Chem., Int. Ed.*, 2002, **41**, 3389–3392.
70 D. A. Dougherty, *Science*, 1996, **271**, 163–168.
71 J. C. Ma and D. A. Dougherty, *Chem. Rev.*, 1997, **97**, 1303–1324.
72 S. Shaik, S. P. de Visser and D. Kumar, *J. Am. Chem. Soc.*, 2004, **126**, 11746–11749.
73 H. Hirao, H. Chen, M. A. Carvajal, Y. Wang and S. Shaik, *J. Am. Chem. Soc.*, 2008, **130**, 3319–3327.
74 S. D. Straight, J. Andréasson, G. Kodis, S. Bandyopadhyay, R. H. Mitchell, T. A. Moore, A. L. Moore and D. Gust, *J. Am. Chem. Soc.*, 2005, **127**, 9403–9409.
75 F. Xu, E. J. Golightly, K. R. Duke, S. F. Lassen, B. Knusen, S. Christensen, K. M. Brown, S. H. Brown and M. Schülein, *Enzyme Microb. Technol.*, 2001, **28**, 744–753.
76 S. J. Langford and T. Yann, *J. Am. Chem. Soc.*, 2003, **125**, 11198–11199.
77 E. Maligaspe and F. D'Souza, *Org. Lett.*, 2009, **12**, 624–627.
78 N. S. Hush, J. R. Reimers, L. E. Hall, L. A. Johnston and M. J. Crossley, *Ann. N. Y. Acad. Sci.*, 1998, **852**, 1–21.